Overview of plasma-tungsten surfaces interactions on the divertor test sector in WEST during the C3 and C4 campaigns

M. Diez, M. Balden, S. Brezinsek, Y. Corre, N. Fedorczak, M. Firdaouss, E. Fortuna, J. Gaspar, J.P. Gunn, A. Hakola, et al.

▶ **To cite this version:**

M. Diez, M. Balden, S. Brezinsek, Y. Corre, N. Fedorczak, et al.. Overview of plasma-tungsten surfaces interactions on the divertor test sector in WEST during the C3 and C4 campaigns. Nuclear Materials and Energy, 2023, 34, pp.101399. 10.1016/j.nme.2023.101399 . hal-04396242

HAL Id: hal-04396242
https://amu.hal.science/hal-04396242

Submitted on 15 Jan 2024

HAL is a multi-disciplinary open access archive for the deposit and dissemination of scientific research documents, whether they are published or not. The documents may come from teaching and research institutions in France or abroad, or from public or private research centers.

L'archive ouverte pluridisciplinaire **HAL**, est destinée au dépôt et à la diffusion de documents scientifiques de niveau recherche, publiés ou non, émanant des établissements d'enseignement et de recherche français ou étrangers, des laboratoires publics ou privés.

Distributed under a Creative Commons Attribution 4.0 International License

Nuclear Materials and Energy 34 (2023) 101399

Contents lists available at ScienceDirect

Nuclear Materials and Energy

journal homepage: www.elsevier.com/locate/nme

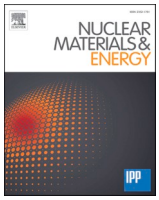

Overview of plasma-tungsten surfaces interactions on the divertor test sector in WEST during the C3 and C4 campaigns

M. Diez [a,*], M. Balden [b], S. Brezinsek [c], Y. Corre [a], N. Fedorczak [a], M. Firdaouss [a], E. Fortuna [d], J. Gaspar [e], J.P. Gunn [a], A. Hakola [f], T. Loarer [a], C. Martin [g], M. Mayer [b], P. Reilhac [a], M. Richou [a], E. Tsitrone [a], T. Vuoriheimo [h], The WEST team [1]

[a] IRFM, CEA, 13108 Saint-Paul-Lez-Durance, France
[b] Max-Planck-Institut für Plasmaphysik, Boltzmannstr.2, 85748 Garching, Germany
[c] Institut für Energie- und Klimaforschung-Plasmaphysik, Forschungszentrum Jülich, Jülich, Germany
[d] Faculty of Materials Science and Engineering, Warsaw University of Technology, PL-02-507 Warsaw, Poland
[e] Aix Marseille University, CNRS, IUSTI, Marseille, France
[f] VTT Technical Research Centre of Finland Ltd, PO Box 1000, FI-02044, VTT, Finland
[g] Aix Marseille University, CNRS, PIIM, Marseille, France
[h] Department of Physics, University of Helsinki, P.O. Box 64, Helsinki 00560, Finland

ARTICLE INFO

Keywords:
WEST
Tungsten
Erosion and deposition
Plasma-wall interactions
Monoblocks

ABSTRACT

Studying the ageing of tungsten monoblocks, their erosion and their fuel inventory is the priority of the WEST post-mortem analyses programme. Actively-cooled ITER-like plasma-facing units (PFUs) and special W-coated marker lower divertor tiles were retrieved from the WEST divertor after the C3 and C4 experimental campaigns to perform ex-situ analyses. The erosion/deposition pattern on the divertor was determined. The deposition is found mainly on the inner side which is covered by layered deposits that increase in thickness in the radial direction from a few hundreds of nm to a maximum of >10 μm. The deposits are mainly composed of W, O, C, B and D coming from transport of W in the vacuum chamber, oxidized layers and boronizations. Traces of Cu, Fe, Mo, Cr, Ag were also detected. A maximum deposition rate of about 1.4 nm/s was estimated while a minimum campaign-averaged net erosion rate of 0.1 nm/s was measured for the erosion markers at the strike line areas. No assessment of the erosion could be done for the W monoblocks due to a lack of diagnostics. However, the W monoblock edges clearly show traces of damage (melting, cracks) when exposed to the parallel heat flux due to relative misalignment of ITER-like PFUs during assembly. Optical hot spots were also evidenced, confirming the numerical simulations, although their impact on the operation and the lifetime of the components was limited.

Introduction

Tungsten (W) has been chosen as the plasma-facing material (PFM) for the divertor of ITER due to its capability to sustain high heat fluxes for long pulses while exhibiting low erosion and low fuel retention. In that framework research studies are currently conducted in W-upgraded tokamaks, i.e., ASDEX Upgrade (W-coated plasma-facing components (PFCs)), JET (ITER-like wall) and EAST (W monoblocks divertors), to better predict interactions between plasma and W PFCs [1–5]. In particular, issues related to material migration (erosion, transport, redeposition) and the modification of W material properties are conducted because they drive the lifetime of the components and the safe operation of a tokamak.

WEST is also a full W environment upgraded tokamak. During phase I (2017–2021), WEST has operated with a divertor equipped with W-coated graphite tiles (both standard and erosion marker tiles) and a set of actively cooled ITER-like plasma-facing units (PFUs). The aim was to assess the behaviour of ITER-like tungsten (W) divertor components under combined heat and particle fluxes in an X-point configuration [6]. During each shutdown, a selected number of ITER-like PFUs and W-coated tiles were removed from WEST and subjected to post-mortem analysis to identify erosion/deposition patterns, thickness and content

* Corresponding author.
E-mail address: mathilde.diez@cea.fr (M. Diez).
[1] See http://west.cea.fr/WESTteam.

https://doi.org/10.1016/j.nme.2023.101399
Received 15 December 2022; Received in revised form 20 February 2023; Accepted 22 February 2023
Available online 25 February 2023
2352-1791/© 2023 The Authors. Published by Elsevier Ltd. This is an open access article under the CC BY-NC-ND license (http://creativecommons.org/licenses/by-nc-nd/4.0/).

of co-deposited layers as well as surface modifications. This paper gives an overview of the results obtained so far on the entire targets (no cutting), with the analysis focusing on targets removed after C3 and C4, for which stable discharges, long pulse duration up to ~1 min, a dedicated helium campaign [7] and steady state heat loads up to 6 MW/m^2 on the lower divertor were achieved [8].

Divertor configuration and operating conditions during WEST phase I

Configuration of the divertor test sector

The lower divertor of WEST consists in 12 sectors, each of them containing 38 components toroidally distributed. During phase I, WEST has operated with 3 types of components (see Fig. 1).

(i) Inertially cooled graphite tiles coated with a ~ 12 μm layer of W and an interlayer of Mo, made by a process based on physical vapor deposition (PVD) [9]. They composed most of the lower divertor.
(ii) Among these W-coated tiles, 8 were specifically equipped with marker coatings (1–2 μm W / 100 nm Mo) for erosion investigation [10,11] referred in this paper as erosion marker tiles. These tiles were mounted in one of the 12 sectors, sector Q2A.
(iii) At the same time ITER-like PFUs were progressively installed in sector Q3B, referred in this paper as the divertor test sector. Each ITER-like PFU consists of 35 W monoblocks (MBs) bonded to a CuCrZr tube. The ITER-like PFUs were delivered by six different suppliers from China, Japan and Europe (F4E), each having their own manufacturing processes. While inertially cooled graphite tiles have a 1° toroidal bevel to protect their leading edges, the ITER-like PFUs do not have such a toroidal bevel. Their relative vertical alignment on the sector governs therefore entirely driving the exposure conditions of their leading edge to the parallel heat flux.

The configuration of the divertor test sector during each experimental campaign of phase I is given in Table 1 (ILPi indicates the name of the ITER-like PFUs and PFU#j indicates their toroidal position on the sector) while Fig. 1 illustrates the test sector during C3 and C4, the two campaigns studied in this paper. During the C1 and C2 campaigns, six ITER-like PFUs, ILP1, ILP2, ILP3, ILP4, ILP15, ILP8 were installed in toroidal position #7, 8, 9, 10, 13 and 14, respectively. For the C3 campaign, component ILP15 was removed and 7 other ITER-like PFUs were installed, namely ILP5, ILP6, ILP7, ILP9, ILP10, ILP13, ILP14, leading to a total number of 12 ITER-like PFUs on the sector, including 2 ITER-like PFUs with unchamfered poloidal edges (ILP6 and ILP9). Two additional ITER-like PFUs with unchamfered poloidal edges (ILP11 and ILP12) were installed in position #17 and #18 for the C4 campaign. In order to meet the needs of the experimental program, ILP2, ILP6 and ILP14 had their toroidal position changed during the shutdown between C3 and C4, as indicated in Table 1. ILP1 was removed while ILP15 was installed again. For the C5 campaign, all the tiles installed on the divertor test sector were removed, except for ILP12, and replaced by 37 toroidally-bevelled ITER-like PFUs.

Plasma configuration on the divertor test targets

The toroidal position of the ITER-like PFUs on the divertor test sector was chosen accordingly to plasma loading, with the aim of maximizing

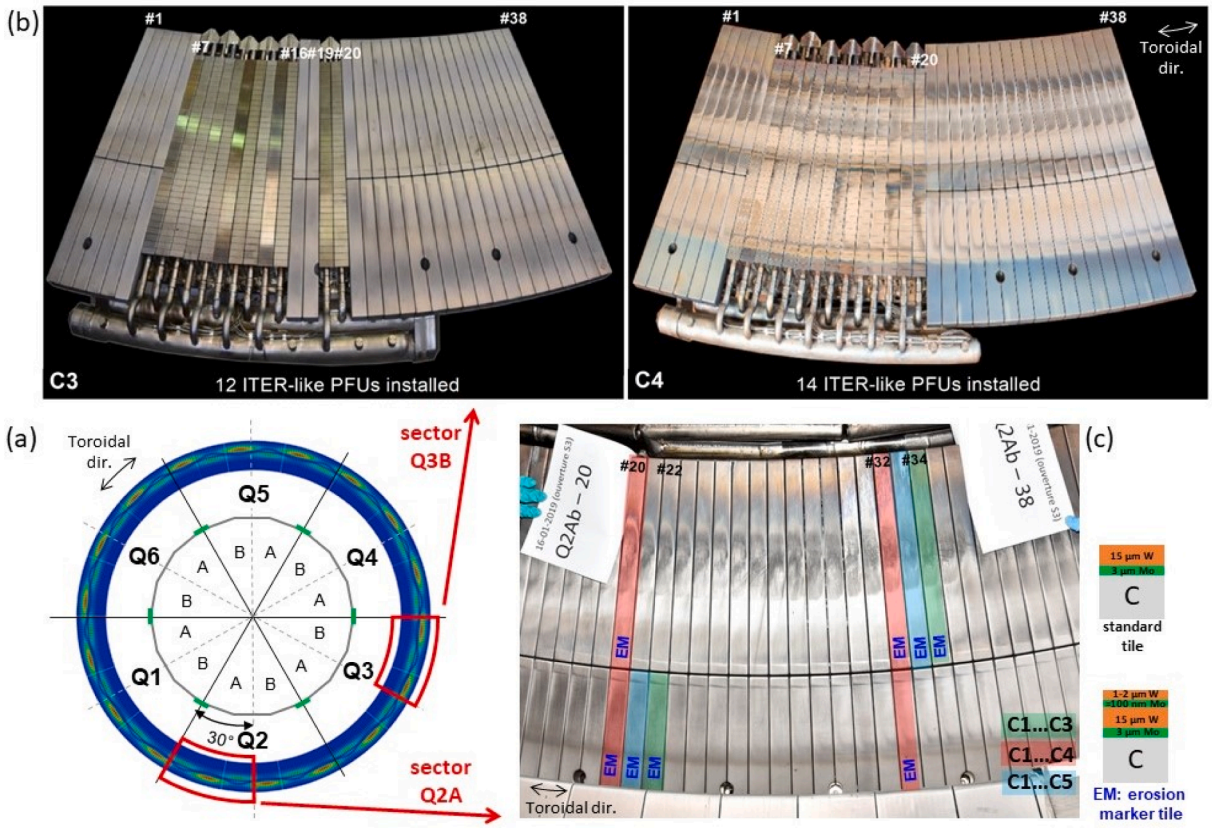

Fig. 1. (a) Top down view of the WEST lower divertor showing the sectors distribution. (b) Photographs of the divertor test sector Q3B taken before C3 (left) and after C4 (right) showing the configuration of the installed ITER-like PFUs. (c) Photograph of sector Q2A equipped with 8 erosion marker tiles retrieved sequentially after C3, C4 and C5. Apart from the erosion markers and the ITER-like PFUs, the lower divertor was composed of standard W-coated graphite tiles.

Table 1
Identification (ILPi) and toroidal position (PFU#j) of the non-beveled ITER-like PFUs installed on the divertor test sector during the first phase of operation of WEST. Unchamfered ITER-like PFUs are indicated by the label 'unch'. ITER-like PFUs with a relative vertical misalignment m_{PFU} exceeding the design specifications of 0.3 mm are also indicated.

	ILP1	ILP2	ILP3	ILP4	ILP5	ILP6 /unch	ILP7	ILP8	ILP9 /unch	ILP10	ILP11 /unch	ILP12 /unch	ILP13	ILP14	ILP15
C1	PFU#7	PFU#8	PFU#9	PFU#10	–	–	–	PFU#14	–	–	–	–	–	–	PFU#13
C2															
C3	PFU#7	PFU#8	PFU#9	PFU#10	PFU#11	PFU#12	PFU#13	PFU#14	PFU#15	PFU#16	–	–	PFU#19	PFU#20	–
C4	m_{PFU}>spec –	PFU#12	PFU#9	PFU#10	PFU#11	m_{PFU}>spec PFU#8	PFU#13	PFU#14	PFU#15	PFU#16	PFU#17	PFU#18	m_{PFU}>spec PFU#19	PFU#7	PFU#20
C5	–	–	–	–	–	m_{PFU}>spec –	m_{PFU}>spec –	–	–	–	m_{PFU}>spec –	PFU#8	m_{PFU}>spec –	–	–

heat and particle fluxes deposited onto their top surface. As shown in Fig. 2b, the plasma pattern obtained by simulation using PFCFlux code [12] on the test sector consists in maximum and minimum heat loads areas alternating on the high field side (HFS) and low field side (LFS) due to the ripple effect. The ITER-like PFUs installed in toroidal position #7–20 benefited from 2 maximum heat loading, one in the HFS and one in the LFS, referred as max inner strike point (ISP) and max outer strike point (OSP), respectively. In these areas, the angle of incidence α of the magnetic field lines is 2–3°. Also, one same tile has two strike points (SP). It must be noted that in WEST, as in a number of tokamaks [13], there is an inner/outer asymmetry in the divertor profiles, which gives rise to higher steady state loads on the LFS (max OSP). This inner/outer asymmetry has been evaluated with a ratio of 1/4 and 3/4, respectively [8].

All radial positions on divertor tiles are described using the so-called s-coordinate system, starting at the inner end of the W-coated graphite tiles and following the tile surfaces from the HFS to the LFS (Fig. 2a). The direction of the plasma flux at the ISP and OSP is indicated by the arrows, allowing therefore to define the trailing and leading poloidal edge of the divertor targets directly exposed to the parallel heat flux (Fig. 2c).

Operating conditions

The ITER-like PFUs and the erosion marker tiles were exposed to C1 to C4 campaign. However, the investigation focuses in this paper on C3 and C4 only as C1 and *C*2 was devoted to developing plasma scenario and plasma control in the new full tungsten configuration of WEST, i.e., low particle and power loads.

Over the course of campaigns C3 and C4, the divertor targets were exposed to about 13,900 *sec*, or ~ 3 h50, of plasma in lower single-null operated in L-mode (2113 shots > 1 s ≈ approximate time to form the X-point) with heating power varying from 1 to 8.8 MW (combining lower hybrid and ion cyclotron resonance heating).

Despite a significant number of transients (>2000 disruptions), 7.5 GJ was conducted to the lower divertor through the monoblocks located in the SP areas, see Fig. 3. They range from s = 220–270 mm (MB 14–17) at the ISP and s = 330–420 mm (MB 23–29) at the OSP due to the different X-point heights used. In these areas, typical values of T_e ~ 20–30 eV and $n_e \sim 3.5.10^{19}$ m^{-3} were reached. MBs located at the OSP were subjected to significant heat loads up to 6 MW/m^2 on their top surface.

The campaigns were run with deuterium except for the last week of C4 for which helium (He) was used (~45 min. plasma operation). The objective of the He campaign was to investigate the effect of helium on tungsten modifications, and specifically to reach the required conditions to form W fuzz in OSP area on W coated graphite tiles. An overview of the He plasma scenario is given in [7].

Post-exposure PFCs characterization

Local modification of ITER-like PFUs

Visual inspections of the ITER-like PFUs after the C3 and C4 campaigns have allowed to identify 3 types of surface modifications on the targets:

- W cracking and melting on exposed leading edges
- Optical Hot Spots
- Arcing

W cracking on exposed leading edges

During the assembly of the targets on the test sector, some ITER-like PFUs were vertically misaligned. Since their leading edges were not protected by the toroidal bevel, this vertical misalignment dominated the impact of the plasma on the tungsten MBs, which were thus directly

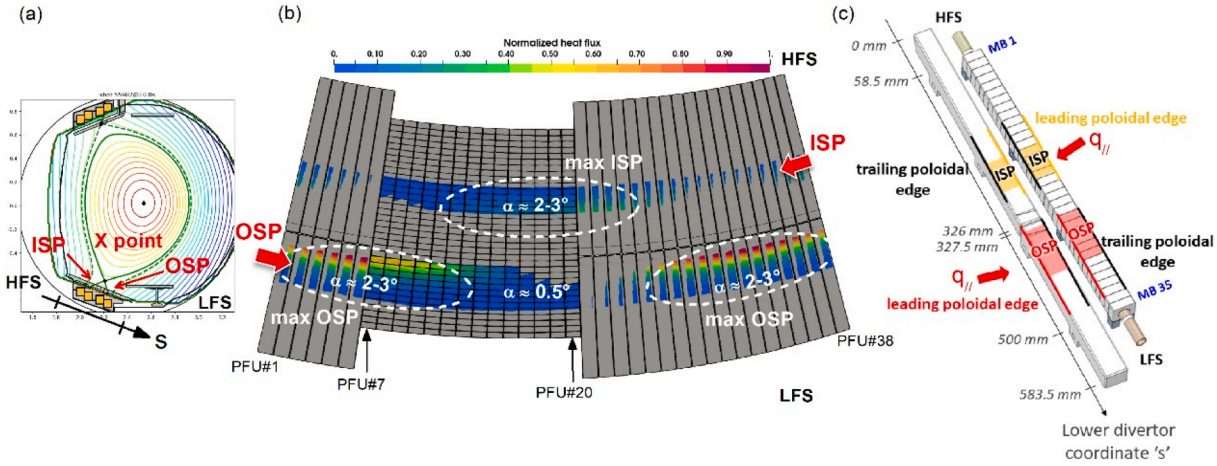

Fig. 2. (a) Cross-section view of WEST showing the poloidal magnetic field configuration (HFS = high field side / LFS = low field side). The s-coordinate (in mm) starts at the inner end (HFS) of the graphite divertor tiles and follows the radial direction on the surface of the tiles. (b) modulated heat load pattern simulated by PFCFlux on the divertor test sector during C4 due to the ripple effect. α indicates the incident angle of the magnetic field lines striking the divertor. (c) W-coated tiles are between s-coordinates 0 mm and 583.5 mm; ITER-like PFUs between s-coordinates 58.5 mm and 500 mm. Black lines indicate trailing (shadowed) poloidal edges of the targets while yellow and red lines indicate leading (wetted) poloidal edges of the targets at the ISP and OSP, respectively. (For interpretation of the references to colour in this figure legend, the reader is referred to the web version of this article.)

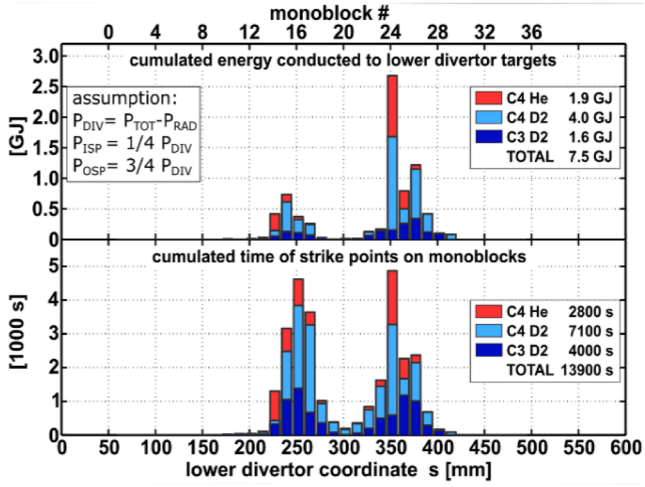

Fig. 3. (top) Cumulated energy conducted to the lower divertor through the strike points, taking the assumption of 1/4 in ISP and 3/4 in OSP. (bottom) cumulated time of plasma on the lower divertor targets during C3 and C4, calculated from the magnetic reconstruction.

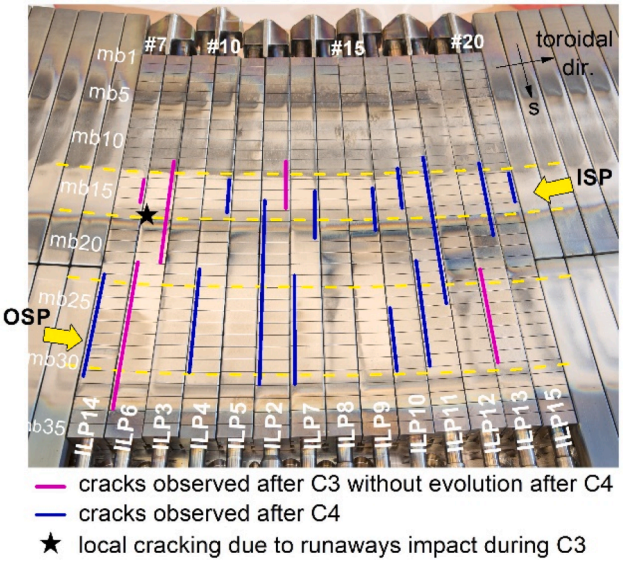

Fig. 4. About 27% of the tungsten monoblocks installed in the divertor test sector had cracks at the end of the c4 campaign. cracks were mainly observed on the leading edges of misaligned ITER-like PFUs but also sometimes on the trailing edges and in the private flux area.

exposed to the parallel heat flux.

As reported in [14,15], regularly spaced cracks of 0.4 mm were observed on the leading edges of misaligned ITER-like PFUs for both chamfered and unchamfered components. The cracks were visible on the top surface of the MBs (propagating in the toroidal direction) as well as on their poloidal side surfaces.

At the end of the C3 campaign, 5 of the 12 ITER-like PFUs installed on the divertor had cracks on their ISP/OSP leading edges (including ILP1 which was removed after C3 and does not appear in Fig. 4). At the end of C4, 10 out of 14 ITER-like PFUs were cracked. The monoblocks affected by cracks are marked in Fig. 4. It represents 133 out of 490 tungsten monoblocks (~27 %). Based on a statistical post-processing of microscopic images, the length of the cracks in the toroidal direction on the top surface of the monoblocks was determined to be between 100 and 1200 μm. A complete study on the morphology of cracks is currently ongoing.

The mechanism of W cracking is not yet well understood. Nevertheless, cracks were observed (i) in regions near the strike points where parallel heat flux is well below the specifications for which the ITER-like MBs were developed (estimated at 40–50 MW/m^2 during C3 for a peak heat load of ~ 2.5 MW/m^2 perpendicular to the top surface and 70–90 MW/m^2 during C4 for a peak heat load of ~ 6 MW/m^2 [8,16]), (ii) sometimes on the trailing edges (ILP2, ILP11) and (iii) in the private flux area (ILP2, ILP6, ILP11, ILP13). In addition, (iv) the ITER-like PFUs with cracks after C3 and still misaligned during C4 do not show any crack propagation or additional cracks, suggesting that the cracks are quite stable once they formed.

Keeping in mind that more off-normal events occur in C3 campaign then in C4, it could be speculated that cracks do not originate from steady-state plasma but would rather originate from transient high heat flux events, such as disruptions.

During phase I, no thermocouples or fiber Bragg gratings were installed on the ITER-like PFUs. The temperature of the W monoblocks

during the operation could only be assessed from the images of the VHR IR (Very High Resolution Infra Red) system. For a 0.2 mm misaligned monoblock it has been evaluated to be between 300 °C and 400 °C on the top surface, right above the cooling pipe, and close to 800 °C on the chamfered poloidal edge during steady-state for heat loads of about 5 MW/m^2 [17].

In the event of a disruption, the temperature of the W monoblocks, and more particularly that of misaligned poloidal edges, will then quickly rise from 70 °C (base temperature in the vacuum vessel) to temperatures far above the ductile–brittle transition temperature (DBTT) and probably up to the recrystallization temperature (1400–1500 °C). A simulation work has shown that this type of thermal cycling across the DBTT can be responsible for high levels of stress which, during the cooling phase, become higher than the yield strength of the material, leading to brittle failure [18].

The operation of WEST has not been hampered so far by W cracking, nor has EAST [19]. But the long-term ageing of the divertor and the impact on its ability to extract heat on the long term are still unknown.

Surface modification of the MB poloidal sides

The operation of WEST has also revealed for the first time the presence of localized hot spots on the tungsten MBs, exactly where numerical predictions had placed them [20]. These hot spots, also called Optical Hot Spots (OHS), are local plasma-wall interaction patterns that result from the penetration of charged particles into the toroidal gaps of the ITER-like PFUs before striking the MB poloidal side on its leading edge of the next PFU. These patterns, where deposited heat flux is high, were found at the images of the toroidal gaps of the upstream MBs for both chamfered and unchamfered ITER-like PFUs. After C3 campaign, OHS were visible on the poloidal side of the MBs on their leading edge [21].

During C4 campaign, an effort was made to better align toroidal gaps between neighbouring PFUs but OHS still formed on the monoblocks. This re-alignment of toroidal gaps allowed to see two OHS on the poloidal side of the same monoblock, the OHS from C3 and the one from C4.

While the two OHS were clearly visible in areas far from the strike points, they were more difficult to see them in the ISP and OSP areas (see Fig. 8 of [14]). Optical observations carried out during post-mortem analysis have indeed revealed the presence of deposited layers on the poloidal sides of the ITER-like PFUs, partially covering the OHS formed in C3. First measurements conducted after C4 by confocal microscopy showed deposits of 2–8 μm thickness on the poloidal side of MB 26 ILP6 while deposits of 100 nm up to 8 μm thickness were also measured by SEM/FIB on the poloidal sides of the erosion marker tiles. These are preliminary results only and need to be investigated into more details during post-mortem analysis of WEST PFCs. Nevertheless, these observations clearly indicate plasma interactions in the vicinity of poloidal gaps.

The presence of OHS did not impact the operation of WEST but they are an important result for ITER because it highlights the fact that even adequate ITER-like PFU assembly procedures cannot eliminate the risk of OHS formation. The question now remains whether the same process will occur on the ITER divertor targets for which a toroidal bevel is present. Like cracking, the evolution and the impact of OHS on the long term on the performance of the plasma is difficult to evaluate but some answers should raise during WEST phase II for which the divertor, fully equipped with toroidally-beveled MBs, will be exposed to long discharges and more campaigns.

Erosion and redeposition pattern on the divertor targets

The erosion/redeposition pattern on the WEST divertor was reconstructed from the various observations made on the top surface of both ITER-like PFUs and erosion marker tiles by imaging and compositional techniques described in the following paragraphs. Fig. 5a illustrates the obtained pattern on the divertor targets along the radial direction. It consist of:

1. erosion in the SP areas (s = 220–270 mm at ISP, s = 328–420 mm at OSP), in good agreement with the magnetic reconstruction presented in Fig. 3.
2. strong deposition in the HFS area (s = 108–220 mm), adjacent to the ISP erosion area. The frontier between these two regions is very clear and sharp and is located on MB 13 (s = ~210 mm), as illustrated in Fig. 5b.
3. thin deposition over the rest of the surfaces, more particularly on the inner and outer ends of the tiles. Besides, rainbow coloured thin films were observed on MB 18 (s = ~275 mm) and MB 32–33 (s = 446–470 mm), marking the end of the SP erosion areas on the LFS side.

Thickness and morphology of the deposited layers

The deposits in the HFS area are stratified layers having each a

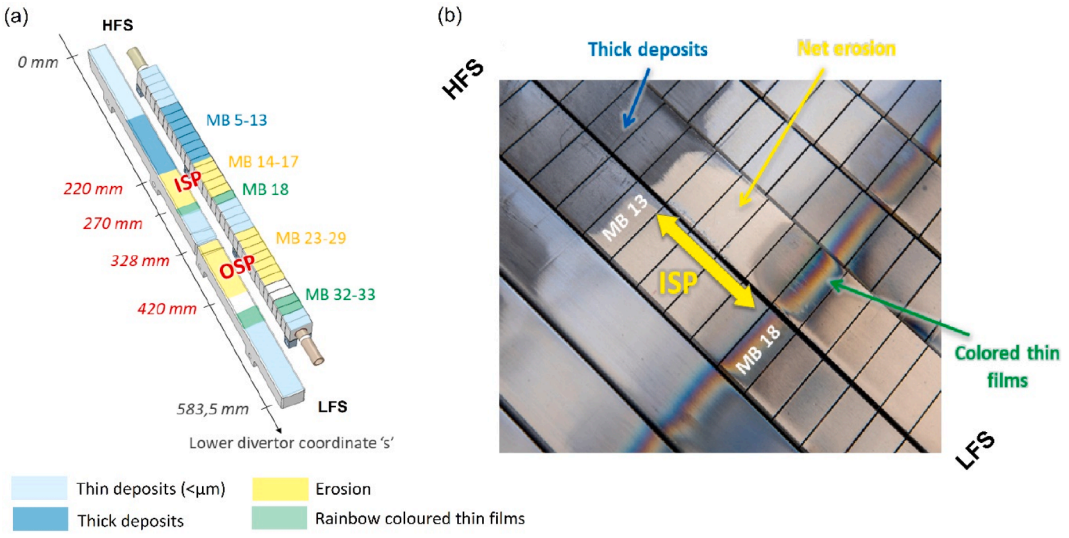

Fig. 5. (a) erosion/redeposition pattern identified on the divertor targets along the radial direction during WEST phase I. (b) photograph of the divertor test sector taken after C4 showing sharp transitions between the dark coloured deposited layers in the HFS area, the erosion-dominated ISP area and the rainbow coloured thin films.

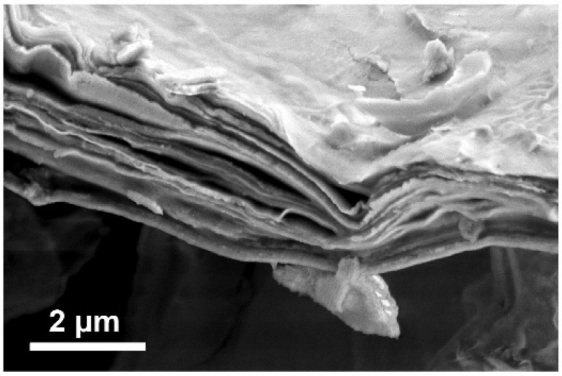

Fig. 6. Layered structure of partially delaminated deposit on ilp4 after c3.

different texture, thickness and composition suggesting a gradual formation over the operation (Fig. 6). The same structure was found for the deposit on the surface of the ITER-like PFUs and the erosion marker tiles [10,22]. Such a stratified structure was observed in other devices [23–25].

The campaign-integrated thickness of the deposits in the radial direction was measured utilizing 4 erosion marker tiles extracted after C3 and C4 as well as 3 ITER-like PFUs with different exposure conditions in terms of campaign history and toroidal position in the sector. The results are depicted in Fig. 7a and represent measurements made using SEM/FIB on the whole tiles and on samples, as well as confocal microscopy after the deposits were detached from the surface using a tape-stripping method [22].

Although these techniques have their own resolution and operate at a local scale, the collected data give a global insight in the erosion/deposition pattern in the divertor. Deposited layers are thin (<1 μm) at the very inner end of the divertor but their thickness rapidly increase to 2 μm around s = 100 mm and continue to grow gradually with s-coordinate. The thickest layers were deposited in the area s = 160–170 mm (MB 9) with thicknesses > 10 μm. Considering that 3 h50 of plasma were performed during C3 and C4, a maximum campaign-averaged deposition rate of ~ 1.4 nm/s can be reached.

Looking at the values more closely, it appears that the erosion marker tiles exposed to C1-C4 have redeposited layers of 14–16 μm while ILP3 has thinner layers, in the order of 10 μm, for the same exposure history. This may be due to the fact that the measurements made by confocal microscopy on ILP3 (and ILP11) minimize the values in the case the deposit did not fully detach from the surface during tape-stripping. Besides, ILP11 shows deposits of similar thickness compared to the other

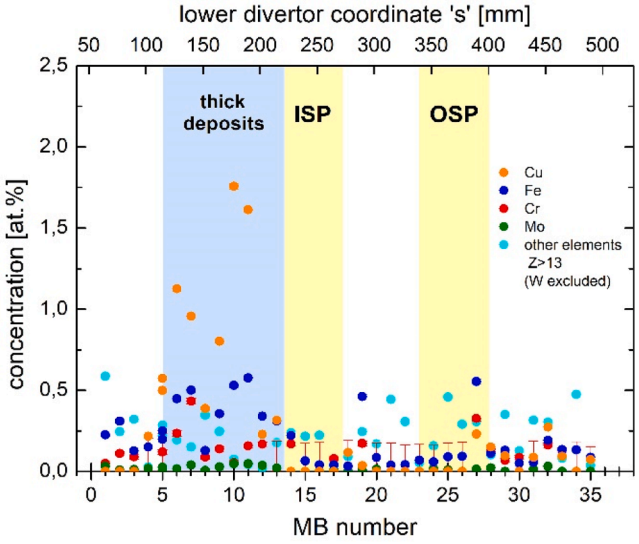

Fig. 8. Main impurities content measured by xrf along the radial direction of iter-like pfu ilp2 after exposure to c1-c4.

two PFUs ILP3 and ILP7 despite the fact that it was exposed to C4 only.

The erosion analysis programme in WEST is not fully completed but these observations indicate that there is still much to be understood about the thickness variation of the deposits.

For the erosion marker tiles, the values of the deposit thickness are organized in 3 categories according to the surface topography. Indeed, the roughness in terms of the arithmetical mean deviation is around R_a = 2–3 μm for the erosion marker tiles (vs R_a ~ 1 μm for the ITER-like PFUs), forming small hills and valleys at the surface of the tiles. The erosion/deposition pattern is then generally not uniform in the strike point areas. Deposited layers remain in the valleys, while hills are more exposed to the plasma, and therefore to erosion, as illustrated in Fig. 7b with a cross-section image of the erosion marker taken at the ISP after C3.

The erosion in the strike points was estimated using IBA analyses computed to plasma duration. A minimum campaign-averaged net erosion of > 0.1 nm/s was assessed [10]. This value is in the same range than the net erosion rate observed in ASDEX Upgrade [26] in a W-environment, with the difference that ASDEX Upgrade operates with ELMs unlike WEST. Since ELMs are a major contribution to W erosion in all other devices (AUG, JET, EAST), here the W sputtering seems very important for operation without transients. This suggests a high

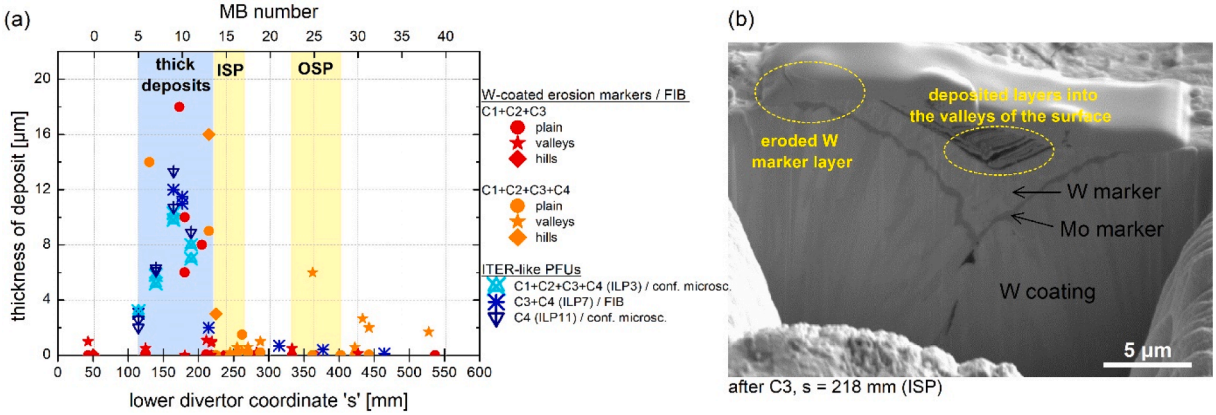

Fig. 7. (a) thickness of redeposited layers along the radial s-coordinate of the divertor targets. The data were obtained on the central line of post-C3, post-C4 erosion marker tiles and ILP7 using SEM/FIB. Confocal microscopy was also used on ILP3 and ILP11 after the deposits were removed by adhesive tape. (b) SEM/FIB image of post-C3 erosion marker tile showing the competition between erosion and redeposition in areas close to the SP due to the roughness of the tiles.

concentration of impurities in the plasma dominating the erosion [27,28]. Finally, it should be noted that this net erosion rate of ~ 0.1 nm/s could only be determined for the W-coated erosion marker tiles. No assessment of erosion was made for the bulk W ITER-like PFUs during the first phase of WEST operation due to the lack of markers or reference on the W monoblocks.

Distribution and composition of the deposited layers

The surface composition of the divertor targets along the radial direction was measured by X-ray fluorescence (XRF). Measurements were made at the centre of each monoblock on ILP2 after exposure to C1-C4, using Olympus Vanta's system with a rhodium X-ray tube, a high voltage of 40 kV and a collimator of 10 mm diameter. With this technique, only elements with Z > 13 are detected. Therefore, the composition of deposits given by XRF presented in Fig. 8 does not include light elements such as B, O, C or D.

The results indicate that the main high Z impurities on the PFU's surface are Cu (LH antennas), Fe and Cr (stainless steel panels) as well as Mo (interlayer coating in the lower divertor graphite tiles). They are mainly found in the region of thick deposits, with a content reaching up to 2 at.%. A non-exposed W sample provided by the same manufacturer than ILP2 was used as a reference and did not reveal the presence of Cu, Fe, Cr and Mo. Therefore, these results clearly evidence that heavy impurities from the main chamber were transported and redeposited in the HFS of the divertor. Ta, Ti and V were also detected on the ITER-like PFU surface with a concentration of about 0.25–0.5 at.% ('other elements with Z > 13' in the figure. This does not include W) but their homogenous repartition along the divertor suggest a different transport mode or origin. For comparison, the value of the reference sample for elements Z > 13 was 0.17 at.%.

The quantification of W in the deposits alone remains difficult to assess. However, the presence of W in the redeposited layers was confirmed during the different characterizations (EDS on the surface, on FIB cross-sections and on TEM cross-sections) and is more likely coming from other sources in the vacuum chamber because the balance of W within the divertor cannot be completed by redistribution only. ERO simulations have shown for example that the upper divertor could be a source of W impurities and contributes strongly to the contamination of core plasma in WEST [29].

In order to have a complete overview of the deposits content, especially in terms of light impurities, IBA analyses were also carried out on the C3 erosion marker tiles, C4 erosion marker tiles and on ILP7 exposed to C3 and C4. The measurements were made at the tandem accelerator at IPP Garching in an analysis chamber that can accommodate large components. For each position on the central line along the tiles, Rutherford backscattering spectrometry (RBS) and nuclear reaction analyses (NRA) were performed (details of the techniques are given in [10]). The data were then fitted self-consistently using the SIMNRA software to convert count integrals (i.e. intensity) and distribution into the channel into at/cm^2, except for the ITER-like PFU which are evaluated only in the thin-layer limit by scaling the intensity integrals (increased error for thick deposits). The obtained results are presented in Fig. 9 and give the amount of B, O, C and D along the s-coordinate.

Two types of information can be extracted from Fig. 9: the quantification of deposited elements and their distribution, informing about the changes of erosion/redeposition pattern.

First of all, the deposited layers on the HFS of the erosion marker tiles (Fig. 9a) show a clear presence of B, C, O and D, in line with the conditioning and the tokamak environment. Boron contributes largely to the impurities content with an amount of about 1x10^{19} at/cm^2 after C3 and 3–4 times more after C4 which can be explained by the increasing use of boronizations during the first phase of operation of WEST (3 boronizations performed in C3 vs 13 in C4). In total about 63 h of boronizatons were performed, equivalent to ~ 160 g of boron injected into the vacuum chamber.

Similarly, the amount of carbon is multiplied by 3 over the course of

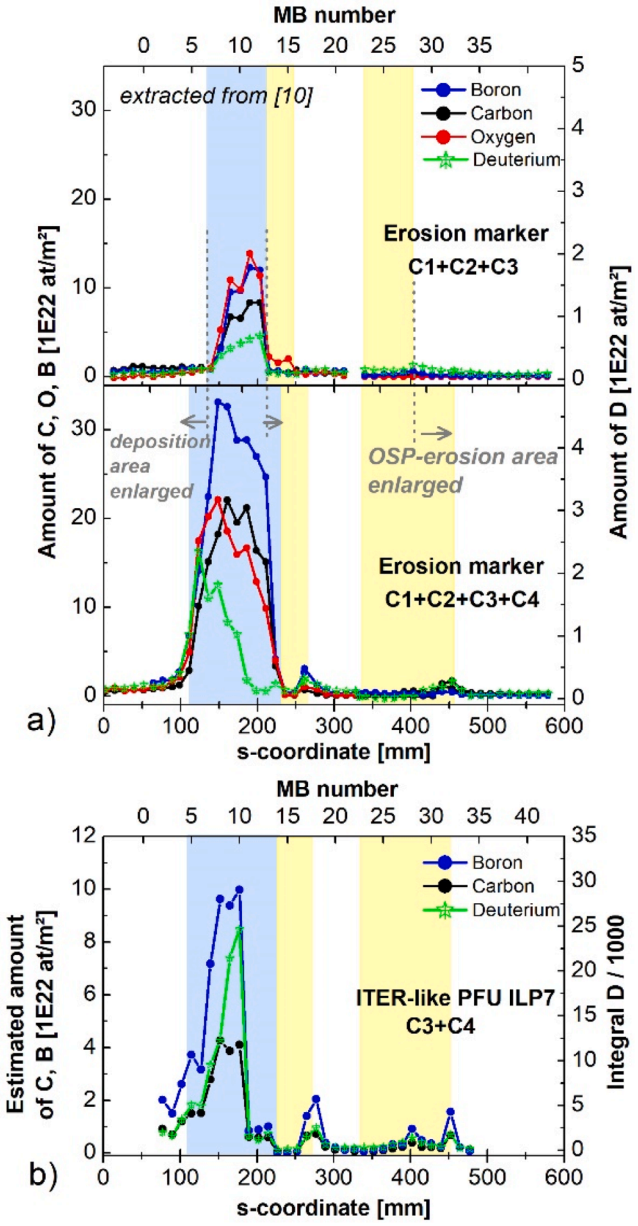

Fig. 9. (a) RBS/NRA analysis showing the amount of B, C, O and D along the post-C3 and post-C4 erosion marker tiles, highlighting changes in the erosion/redeposition pattern between C3 and C4. The data are extracted from [10]. (b) The same analysis was performed on ILP7 exposed to C3 and C4, except that the data were evaluated in the thin-layer limit (increased error for thick deposits). A scaling factor of 8.9 was applied between the y-axis of B and C to take the difference in cross-section into account.

the two campaigns and reaches about 2x10^{19} at/cm^2 after C4 campaign. This could be explained by the delamination and arcing through the coating of the antenna protections and/or inertially cooled divertor tiles that occurred during C3 and C4 [14], exposing the graphite substrate to chemical and physical sputtering by D during C3 and then additionally by He during C4.

The deposited layers also contain oxygen although its quantification was not a direct measurement but was rather fitted to RBS/NRA data with good confidence (presence of O was also confirmed by EDS on the surface and on FIB cross-sections). Oxygen could have been trapped during plasma exposure or could originate from air exposure by the venting or/and during storage of the tiles.

Finally, it can be seen that the total amount of deuterium is

increasing from 0.5x10^{18} at/cm^2 in C3 to about 2x10^{18} at/cm^2 in C4, although these values may be underestimated due to the limitation of depth analysis (3 μm into W and up to 10 μm in the light elements deposits). Deuterium got co-deposited during the layer growth and the fraction of D to all atoms in the layer depends strongly on depositions condition, especially on the temperature which is very hard to predict for such layered structure found on the tiles. The observed fraction is in the reported range for deposited layers [30].

As for the spatial distribution of the elements, it is possible to identify changes in the erosion/redeposition pattern between C3 and C4. The HFS deposition area was enlarged (s = 100–235 mm after C4 vs s = 140–210 mm after C3) as well as the OSP erosion area (s = 330–440 mm after C4 vs s = 330–400 mm after C3). A shift of the ISP erosion area also occurred (s = 235–278 mm after C4 vs s = 217–254 mm after C3). These changes are intrinsically related to the operation and the different positions of the plasma strike points and a good coherency was found between the erosion marker tiles and the ITER-like PFU after C4.

Summary

The WEST post-mortem analyses programme conducted between 2019 and 2022 on the divertor targets is starting to inform the ageing behaviour of the W monoblocks and the erosion/redeposition processes in the WEST tokamak.

Analyses performed on the top surface of the divertor targets clearly show a transport of impurities inside the vacuum vessel towards the HFS of the divertor where plasma is 'cold' (far from the scrape-off layer). In this redeposition area, layers of >10 μm containing typical elements found in tokamak deposits, i.e. C, B, W, Cu, Fe were found after 3 h50 of plasma (max 1.4 nm/s campaign-averaged deposition rate). The sources of impurities are assumed to be the delamination of the W layer of the inertially cooled graphite divertor tiles and/or the antenna protections, sputtering of LH antennas waveguides, sputtering of the stainless steel panels and transport of W from other PFCs. B and D used during conditioning have also largely diffused into the deposits, while a high level of oxygen was also detected, which could either come from the oxidation of the deposited layers during plasma exposure or during ex-situ storage. The retention of helium in W and potential fuzz formation or W structure modification are still yet to be assessed. The deposited layers have a similar composition on both the ITER-like PFUs and the W-coated graphite tiles and exhibit a layered structure, even if the observed thickness variation is not explainable yet. However, the relation with plasma exposure history is difficult to establish.

In the strike point areas, where maximum heat loads of 6 MW/m^2 were reached, erosion occurs as expected, with almost no trace of deposition of light or heavy elements on the target surface. A relatively high net erosion rate (considering that WEST do not operate with ELMs) of at least 0.1 nm/s was measured for the W-coated erosion marker tiles which could be explained by the impurities present in the plasma enhancing W sputtering. The erosion was inhomogeneous on a microscopic scale due to the roughness of the tiles that could impact the erosion/redeposition mechanisms. The erosion assessment of bulk W ITER-like PFUs could not be performed during WEST phase I, but is being considered for phase II during which longer and more pulses will be performed.

As for the MBs ageing, no major damage was observed at the end of the first phase of operation. Nevertheless, 27 % of the 490 MBs installed on the divertor test sector show cracks, sometimes accompanied by local melting. All of them are located on poloidal edges directly exposed to the parallel heat flux in the ISP/OSP areas due to relative misalignment and the absence of a toroidal bevel. Despite these observations and despite the fact that no impact on the operation was observed in WEST, the main question today remains whether tungsten cracking could alter the components lifetime and the ability of the divertor to fulfil its role of extracting power. An important work combining post-mortem analyses and simulation has started to better understand the mechanisms responsible of the cracks formation and evolution. Our current understanding is a brittle cracking of cold W that occurs due to normal stresses exceeding the material yield stress during transients.

CRediT authorship contribution statement

M. Diez: Investigation, Formal analysis, Writing – original draft. **M. Balden:** Investigation, Formal analysis, Writing – review & editing. **S. Brezinsek:** Supervision. **Y. Corre:** Writing – review & editing. **N. Fedorczak:** Formal analysis. **M. Firdaouss:** . **E. Fortuna:** Investigation. **J. Gaspar:** Formal analysis, Writing – review & editing. **J.P. Gunn:** Formal analysis. **A. Hakola:** Supervision, Writing – review & editing. **T. Loarer:** . **C. Martin:** Investigation, Formal analysis. **M. Mayer:** Investigation, Formal analysis. **P. Reilhac:** Investigation. **M. Richou:** Investigation, Writing – review & editing. **E. Tsitrone:** Supervision. **T. Vuoriheimo:** Investigation.

Declaration of Competing Interest

The authors declare that they have no known competing financial interests or personal relationships that could have appeared to influence the work reported in this paper.

Data availability

Data will be made available on request.

Acknowledgments

This work has been carried out within the framework of the EUROfusion Consortium, funded by the European Union via the Euratom Research and Training Programme (Grant Agreement No 101052200 — EUROfusion). Views and opinions expressed are however those of the author(s) only and do not necessarily reflect those of the European Union or the European Commission. Neither the European Union nor the European Commission can be held responsible for them.

References

[1] A. Hakola, et al., Nucl. Fusion 57 (2017), 066015, https://doi.org/10.1088/1741-4326/aa69c4.
[2] R. Neu at al.,, J. Nucl. Mater. 438 (2013) S34–S41, https://doi.org/10.1016/j.jnucmat.2013.01.006.
[3] A. Widdowson, et al., Nucl. Mater. Energy 12 (2017) 499–505, https://doi.org/10.1016/j.nme.2016.12.008.
[4] N. Catarino, et al., Nucl. Mater. Energy 12 (2017) 559–563, https://doi.org/10.1016/j.nme.2016.10.027.
[5] R. Yan, et al., Nucl. Mater. Energy 30 (2022), 101103, https://doi.org/10.1016/j.nme.2021.101103.
[6] M. Missirlian, et al., Fusion Eng. Des. 89 (2014) 1048–1053, https://doi.org/10.1016/j.fusengdes.2014.01.050.
[7] E. Tsitrone, et al., Nucl. Fusion 62 (2022), 076028, https://doi.org/10.1088/1741-4326/ac2ef3.
[8] J. Gaspar, et al., Nucl. Fusion 61 (2021), 096027, https://doi.org/10.1088/1741-4326/ac1803.
[9] M. Firdaouss, et al., Fusion Eng. Des. 124 (2017) 207–210, https://doi.org/10.1016/j.fusengdes.2017.02.087.
[10] M. Balden, et al., Phys. Scr. 96 (2021), 124020, https://doi.org/10.1088/1402-4896/ac2182.
[11] S. Lehto, et al., Fusion Eng. Des. 66–68 (2003) 241–245, https://doi.org/10.1016/S0920-3796(03)00291-6.
[12] M. Firdaouss, et al., J. Nucl. Mater. 438 (2013) S536–S539, https://doi.org/10.1016/j.jnucmat.2013.01.111.
[13] R.A. Pitts, et al., J. Nucl. Mater. 337–339 (2005) 146–153, https://doi.org/10.1016/j.jnucmat.2004.10.111.
[14] M. Diez, et al., Nucl. Fusion 61 (2021), 106011, https://doi.org/10.1088/1741-4326/ac1dc6.
[15] J.P. Gunn, et al., Nucl. Mater. Energy 27 (2021), 100920, https://doi.org/10.1016/j.nme.2021.100920.
[16] A. Grosjean, et al., Nucl. Mater. Energy 27 (2021), 100910, https://doi.org/10.1016/j.nme.2021.100910.
[17] Y. Corre, et al., Nucl. Mater. Energy 34 (2023), 101366, https://doi.org/10.1016/j.nme.2023.101366.

[18] A. Durif, et al., Fusion Eng. Des. 188 (2023), 113441, https://doi.org/10.1016/j.fusengdes.2023.113441.
[19] D. Zhu, et al., Nucl. Fusion 62 (2022), 056004, https://doi.org/10.1088/1741-4326/ac3f48.
[20] J.P. Gunn, et al., Nucl. Fusion 57 (2017), 046025, https://doi.org/10.1088/1741-4326/aa5e2a.
[21] M. Diez, et al., Nucl. Fusion 60 (2020), 054001, https://doi.org/10.1088/1402-4896/ac267e.
[22] C. Martin, et al., Phys. Scr. 96 (2021), 124035, https://doi.org/10.1088/1402-4896/ac267e.
[23] A.T. Peacock, et al., J. Nucl. Mater. 266 (1999) 423–428, https://doi.org/10.1016/S0022-3115(98)00670-9.
[24] T. Dittmar, et al., Phys. Scr. 138 (2009), 014027, https://doi.org/10.1088/0031-8949/2009/T138/014027.
[25] M. Balden, et al., Nucl. Fusion 54 (2014), 073010, https://doi.org/10.1088/0029-5515/54/7/073010.
[26] A. Hakola, et al., J. Nucl. Mater. 463 (2015) 162–165, https://doi.org/10.1016/j.jnucmat.2014.11.034.
[27] G.J. Van Rooij, et al., Phys. Scr. T171 (2020), 014060, https://doi.org/10.1088/1402-4896/ab606c.
[28] C. Klepper, et al., Plasma Phys. Control. Fusion 64 (2022), 104008, https://doi.org/10.1088/1361-6587/ac8acc.
[29] S. Di Genova, et al., Nucl. Fusion 61 (2021), 106019, https://doi.org/10.1088/1741-4326/ac2026.
[30] J. Roth, et al., J. Nucl. Mater. 390 (2009) 1–9, https://doi.org/10.1016/j.jnucmat.2009.01.037.